Supporting Information

High and Tuneable Anisotropic Thermal Conductivity Controls the Temperature Distribution of 3D Printed All-Polyethylene Objects

Ina Klein [a], Thomas Tran [a], René Reiser [b,c], Maximilian Theis [a], Sabine Rosenfeldt [a], Marius Schöttle [a], Carl Schirmeister [b,c], Peter Bösecke [d], Stefan Rettinger [a], Rolf Mülhaupt [b] and Markus Retsch [a, e]

[a.] *Department of Chemistry, Physical Chemistry I, University of Bayreuth, 95447 Bayreuth, Germany.*

[b.] *Freiburg Materials Research Center FMF and Institute for Macromolecular Chemistry, Albert-Ludwigs-University Freiburg, 79104 Freiburg, Germany.*

[c.] *LyondellBasell Industries, Industriepark Höchst, 65926 Frankfurt am Main, Germany.*

[d.] *European Synchrotron Radiation Facility (ESRF), 71 Avenue des Martyrs, CS 40220, 38043 Grenoble Cedex 9, France*

[e] *Bavarian Polymer Institute, Bayreuth Center for Colloids and Interfaces, and Bavarian Center for Battery Technology (BayBatt), University of Bayreuth, 95447, Germany*

Infrared Spectroscopy

Table S1: Broad band infrared spectrum and assignments for 3D printed all-PE material.

Wave number / cm^{-1}	Polarization	Assignment
719	σ	$\gamma_r(CH_2)$ [1,2]
730	σ	$\gamma_r(CH_2)$ [1,2]
908	σ	$\delta(R–CH=CH_2)$ [2]
966	σ	$\gamma_r(CH_3)$, trans RCH=CHR' [2]
991	σ	$RCH=CH_2$ [2]
1051	π	$\gamma_t(CH_2)$ [2]
1082	σ	$\nu(C–C)$ [2]
1177	π	$\gamma_w(CH_2)$ [2]
1188	σ	
1304	π	$\gamma_w(CH_2)$, $\gamma_t(CH_2)$, amorphous [1-3]
1352	π	$\gamma_w(CH_2)$, amorphous [1-3]
1367	π	$\gamma_w(CH_2)$ [1-3]
1464	σ	$\delta(CH_2)$ [1,2]
1472	σ	$\delta(CH_2)$ [1,2]
1819	π	$\nu(C–C) + \gamma_r(CH_2)$ $2 \cdot \delta(R–CH=CH_2))$ [2]
1898	σ	$2 \cdot \gamma_r(CH_2)$ $2 \cdot RCH=CH_2$ (?) [2]
2019	π	$\gamma_t(CH_2) + \gamma_r(CH_2)$ [2]
2243	π	$\gamma_w(CH_2) + \nu(0)$ [2]
2328	σ	$\gamma_w(CH_2) + \gamma_r(CH_3)$ $2 \cdot \gamma_r(CH_2)$ [2]
2345	σ	$2 \cdot \gamma_t(CH_2)$ [2]
2635	σ	$\gamma_r(CH_2) + \delta(CH_2)$ [2]
2660	σ	$\gamma_w(CH_2) + \gamma_t(CH_2)$ [2]
2741	σ	$2 \cdot \gamma_w(CH_2)$ $\delta(CH_2) + \gamma_t(CH_2)$ [2]

~ 2837 – 2862	σ	$\nu_s(CH_2)$[1,2]
~ 2882 – 2941	σ	$\nu_a(CH_2)$ [1,2]
3604	σ	$\nu_a(CH_2) + \gamma_r(CH_2)$ [2]
3643	π	$3 \cdot \gamma_t(CH_2)$ $\delta(CH_2) + \nu(\pi) + \nu(0)$ [2]
~ 4095 - 4195	σ	$\nu_a(B_{1u}) + \gamma_r(A_g)$ $\nu_a(CH_2) + \gamma_t(CH_2)$ [2]
4220	π	$\nu_{as}(CH_2) + \gamma_w(CH_2)$ [4]
4251	σ	$\nu_s(CH_2) + \delta(CH_2)$ [4]
4322	σ	$\nu_{as}(CH_2) + \delta(CH_2)$ [4]
5664	σ	$2 \cdot \nu_s(CH_2)$ [4]
5775	σ	$2 \cdot \nu_a(CH_2)$ [4]

IR spectroscopy of unidirectionally printed all-PE material is applied for polarization angles between 10° and 100°. The values can be extrapolated to angles between 90° and 360°. A peanut shape, typical for the display of Malus' Law, can be fitted.[5] However, the original form of Malus' Law (Formula S1) cannot be fully adopted, as the transmission of the polarized IR frequencies (ν) does not range between 0 and the initial intensity (T_0), but between a minimum (T_{min}) and maximum transmission (T_{max}), thus Malus' Law is adjusted according to Formula S2.1 and S2.2.

Malus' Law	$T(\nu) = T_0(\nu) \, \cos^2(\sigma)$	Formula S1
Parallel polarized frequencies:	$T(\nu) = [T_{max}(\nu) - T_{min}(\nu)] \, \cos^2(\sigma + 90\,°) + T_{min}$	Formula S2.1
Perpendicular polarized frequencies:	$T(\nu) = [T_{max}(\nu) - T_{min}(\nu)] \, \cos^2(\sigma) + T_{min}$	Formula S2.2

The adjusted Malus' Laws show that the change in transmission is proportional to the squared cosine of the angle σ, whereby σ is the deviation between print direction and light polarization.

Wide Angle X-Ray Scattering and X-Ray Diffraction
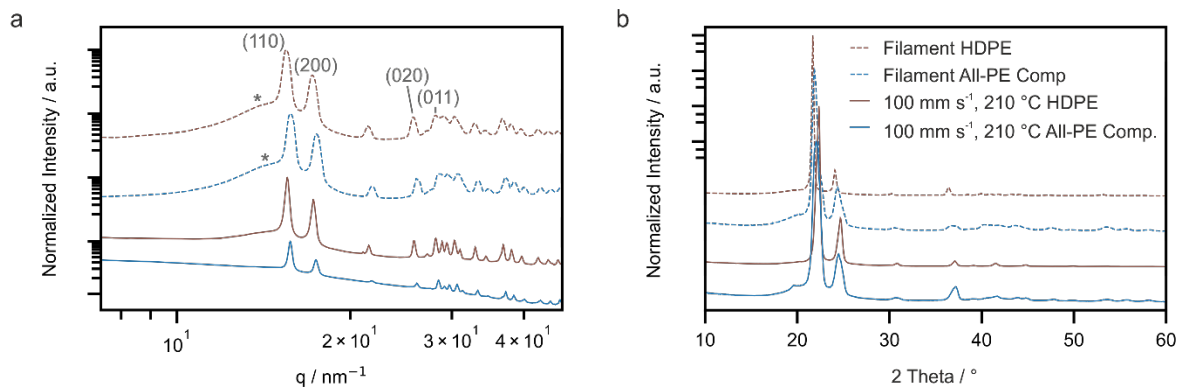
Figure S1: Spectra of the benchmark HDPE filament, all-PE filament and therewith 3D printed samples. The lattice planes (110), (200), (020) and (011) of orthorhombic PE are labeled.[6] a) WAXS measurements performed in transmission geometry b) XRD measurements performed in Bragg-Brentano geometry and spinning mode.

In agreement with the literature, WAXS and XRD spectra reveal mainly orthorhombic PE crystal cells of the space group Pnam.[6] Furthermore, the measured data exhibit a weak signal for both filaments at around 14 nm^{-1} (asteriscs in Fig. S1 a), which diminishes by processing the materials by FFF. The signal can be based on amorphous PE and small amounts of the (010) plane of monoclinic crystallized PE. Both amorphous and monoclinic PE could be converted into the orthorhombic PE phase due to the melting and recrystallization process of FFF.

To describe the orientation of the PE chains more quantitatively the Hermans factor f_H is calculated using the azimuthal angle (ψ) dependent diffraction intensities ($I(\psi)$) corresponding to the hkl planes (200) and (020).[7, 8] The azimuthal plots are exemplary shown for printed all-PE material in Figure S2.
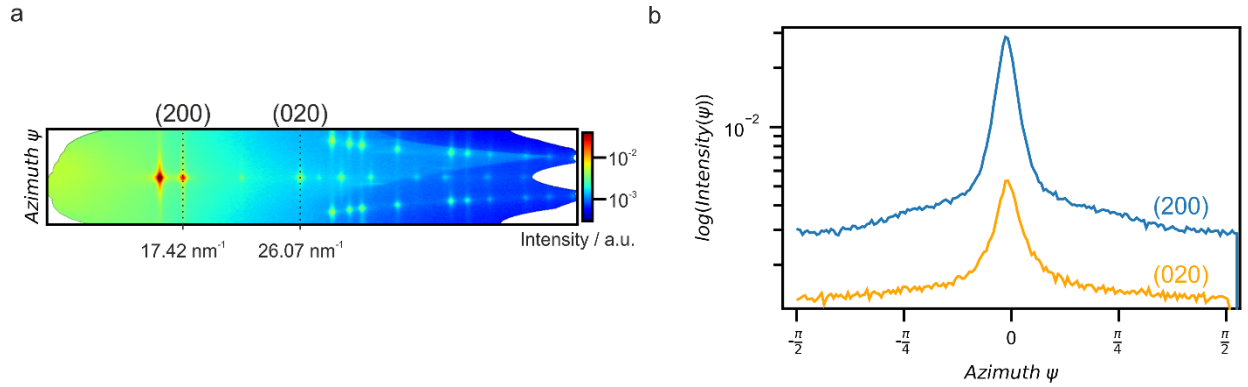
Figure S2: Wide angle X-ray scattering data of all PE material printed with 100 mm s^{-1} and 210 °C a) 2D Azimutal representation with indication of the hkl planes (200) and (020). b) Scattering intensity $I(\psi)$ vs. azimuth angle ψ for the hkl planes (200) and (020).

In a first step $\overline{\cos^2(\phi)}$ is calculated according to Formula S3 and S4. Hereby ϕ are the angles formed by the crystallographic axes a, b and c and θ represents the Bragg angle of the respective hkl plane.

$$\overline{\sin^2(\psi)} = \frac{\int_0^{\pi/2} I(\psi) \sin^2(\psi) \cos(\psi) \; d\psi}{\int_0^{\pi/2} I(\psi) \cos(\psi) \, d\psi} \qquad \text{Formula S3}$$

$$\overline{\cos^2(\phi)} = \cos^2(\theta) \; \overline{\sin^2(\psi)} \qquad \text{Formula S4}$$

The calculations are performed for all-PE filament, HDPE filament and therewith printed samples using a print temperature of 210 °C and a print speed of 100 mm s^{-1}.

Table S2 provides the Bragg angles θ and the values obtained for $\overline{\cos^2(\phi)}$.

Table S2: Bragg angles θ and calculated $cos^2(\phi)$ for all-PE filament and HDPE filament and therewith 3D printed samples.

Sample	hkl	θ / °	$\overline{\cos^2(\phi)}_a$	$\overline{\cos^2(\phi)}_b$
HDPE Filament	200	7.981	0.296	
	020	11.994		0.330
Printed HDPE	200	8.011	0.348	
	020	12.034		0.287
All-PE Filament	200	8.118	0.356	
	020	12.153		0.209
Printed All-PE Material	200	8.099	0.177	
	020	12.172		0.239

In a next step the orientation factors f_a and f_b can be calculated using Formula S5 and finally the Hermans factor f_H, which is equal to f_c, can be obtained *via* Formula S6.

$$f_a = 0.5 \left(3 \; \overline{\cos^2(\phi)}_a - 1 \right)$$

Formula S5

$$f_b = 0.5 \left(3 \; \overline{\cos^2(\phi)}_b - 1 \right)$$

$$f_H = f_c = -f_a - f_b$$

Formula S6

The Hermans orientation factor f_H is - 0.5 in the case of perpendicular orientation, 0 for isotropic conditions and 1 for perfect parallel orientation of the chains in the print direction. The resulting orientation factors, obtained from one thin film specimen per sample, are summarized in Table S3.

Table S3: Orientation factors f_a, f_b and f_c calculated for all-PE filament and benchmark HDPE filament and therewith 3D printed samples.

Sample	f_a	f_b	$f_c = f_H$
HDPE Filament	- 0.06	0.00	0.06
Printed HDPE	0.02	- 0.07	0.05
All-PE Filament	0.03	- 0.19	0.16
Printed All-PE Material	- 0.23	- 0.14	0.37

A comparison of WAXS measurements of printed all-PE material with various print temperatures and print speeds is applied to investigate the effect of print parameters on the crystal structure.
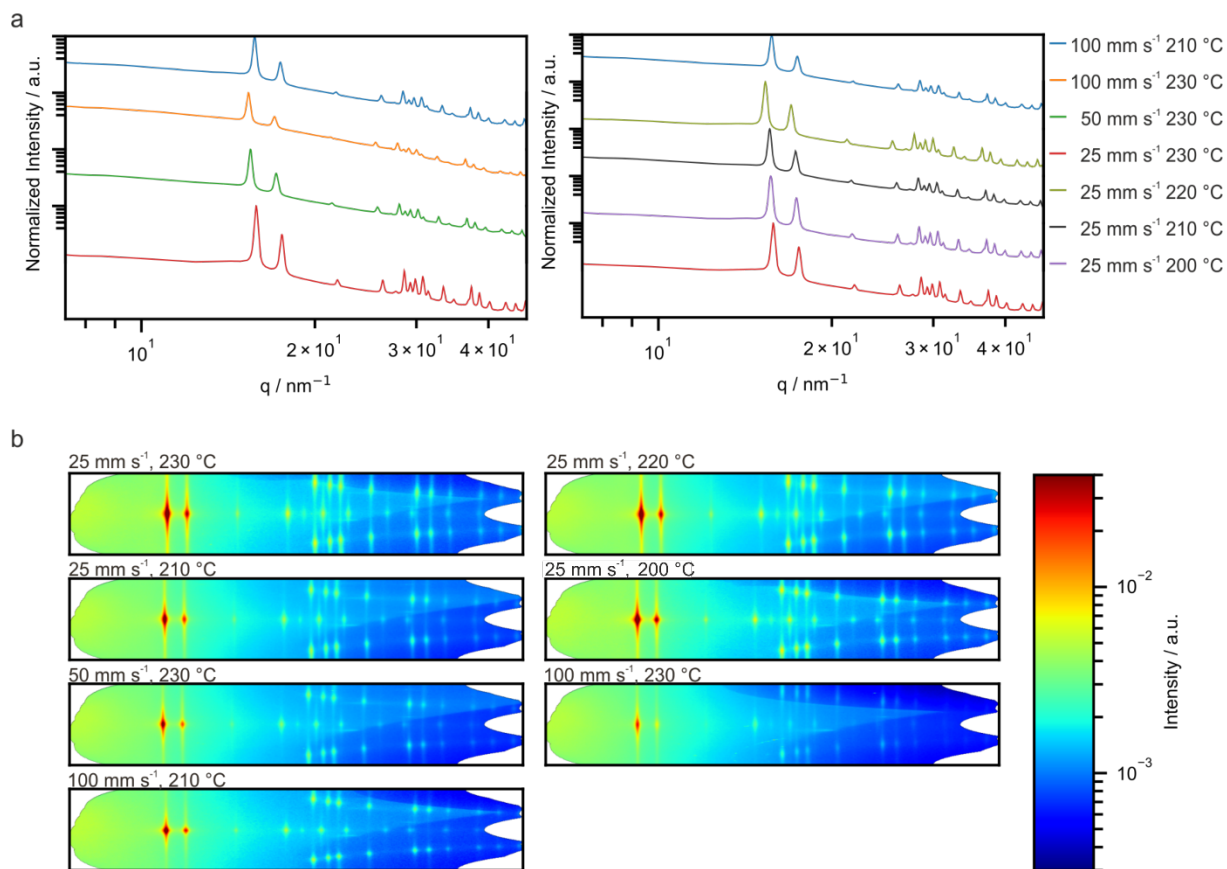
Figure S3: WAXS of all-PE material processed by FFF with various print temperatures and print speeds a) 1D WAXS spectra. b) 2D WAXS patterns (azimuth vs. momentum transfer).

Table S4: Orientation factors f_a, f_b and f_c calculated for all-PE material printed with various print temperatures and print speeds.

Sample	f_a	f_b	$f_c = f_H$
25 mm s⁻¹ 230 °C	-0.21	-0.16	0.37
25 mm s⁻¹ 220 °C	-0.23	-0.16	0.39
25 mm s⁻¹ 210 °C	-0.20	-0.14	0.34
25 mm s⁻¹ 200 °C	-0.25	-0.17	0.42
50 mm s⁻¹ 230 °C	-0.16	-0.11	0.27
100 mm s⁻¹ 230 °C	-0.10	-0.09	0.19
100 mm s⁻¹ 210 °C	-0.23	-0.14	0.37

Figure S3 a and b show that neither the position of Bragg reflexes in 1D WAXS spectra, nor the 2D WAXS patterns significantly depend on print speed or print temperature used in our work. Furthermore, the Hermans factors, calculated from the WAXS spectra, do not indicate an unambiguous trend (Table S4). We note that all Hermans factor calculations were based on a single thin film specimen as shown in Fig. S3. Additional specimens for each combination of print speed and temperature should be measured to assess the accuracy of the Hermans factor calculation. Nonetheless, it is observable that the Hermans factors for all printed all-PE material samples indicate a PE chain alignment in the print direction.

The lattice parameters of the orthorhombic crystals are determined *via* Formula S7 for the corresponding lattice planes (110), (200), and (011).[6]

$$\frac{1}{d_{hkl}} = \frac{h^2}{a^2} + \frac{k^2}{b^2} + \frac{l^2}{c^2} \qquad \text{Formula S7}$$

The experimental lattice parameters are determined to a = 0.72 nm − 0.74 nm, b = 0.48 nm − 0.49 nm and c = 0.24 nm − 0.26 nm. These values are in agreement with the results found by Schirmeister *et al.*[9]

Small Angle X-Ray Scattering
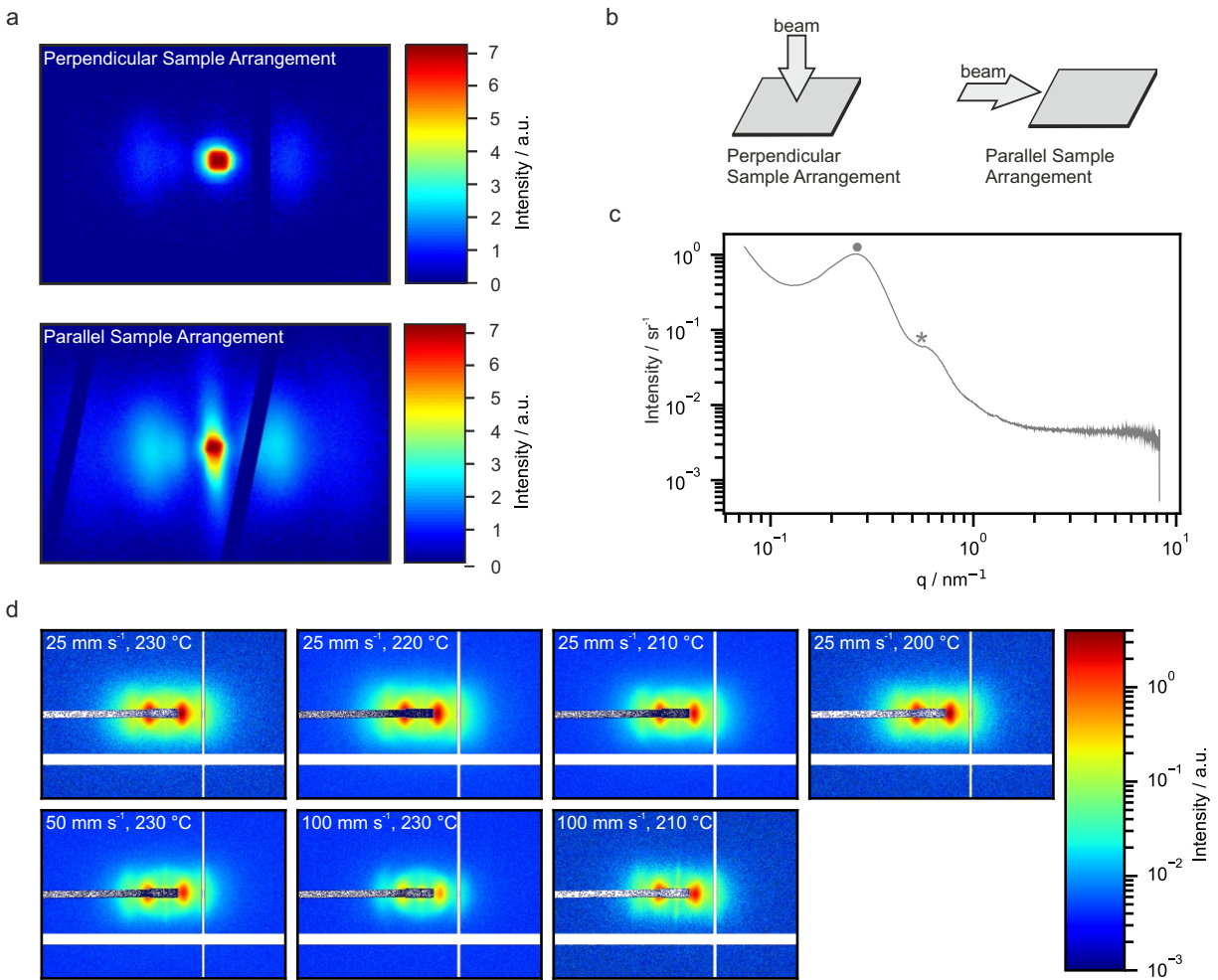
Figure S4: 2D SAXS of all-PE material processed by FFF (detector coordinates q_y vs. q_x) a) with a print speed of 100 mm s^{-1} and a print temperature of 210 °C measured by a lab-based *Double Ganesha AIR* system; Measurements performed perpendicular to the sample and parallel to the sample. b) Schematic illustration of the perpendicular and parallel arrangement of the beam and sample. c) 1D SAXS spectrum of all-PE material printed with 25 mm s^{-1} and 230 °C. The maximum (•) and faintly pronounced minimum (*) used to estimate the lamellar thickness and inter-lamellar distance, respectively, are indicated d) 2D SAXS of all-PE material processed by FFF with various print temperatures and print speeds.

Figure S4 a show the signals obtained with a lab-based system. The reflexes associated with shish-kebab crystal structures are significantly better visible when measured parallel to the printed layer compared to perpendicular arrangement of the beam and the printed layer (Figure S4 b). Note that in the case of perpendicular arrangement, the scattering contribution of the shish structures is not detectable, and the kebab structures solemnly provide a weak signal. Measurements *via* a high brilliance beamline provide a better resolution and allow fast measurements in the perpendicular arrangement. Both scattering

contributions of shish and kebab structures are easily detected. In contrast to our expectations, the 2D SAXS patterns are not significantly dependent on print speed or print temperature in the investigated parameter range (Figure S4 d). The SAXS data are furthermore used to estimate the thickness of the HDPE lamellae from a faintly pronounced local minimum (marked *****) at around 0.48 nm^{-1} and the inter-lamellar distances from a maximum (marked •) at roughly 0.26 nm^{-1}.

Table S5: Lamellar thicknesses and inter-lamellar distances of shish-kebab crystals in all-PE material processed by FFF with various print temperatures and print speeds and in all-PE filament.

Print Parameters	Thickness of lamellae / nm	Inter-lamellar distance / nm
Filament	13	24
100 mm s^{-1} 210 °C	13	24
100 mm s^{-1} 230 °C	13	23
50 mm s^{-1} 230 °C	13	25
25 mm s^{-1} 230 °C	14	27
25 mm s^{-1} 220 °C	13	27
25 mm s^{-1} 210 °C	13	25
25 mm s^{-1} 200 °C	13	26

The inter-lamellar distance appears to decrease slightly with increasing print speed, whereas no significant trend can be observed for the variation of the print temperature.

Differential Scanning Calorimetry
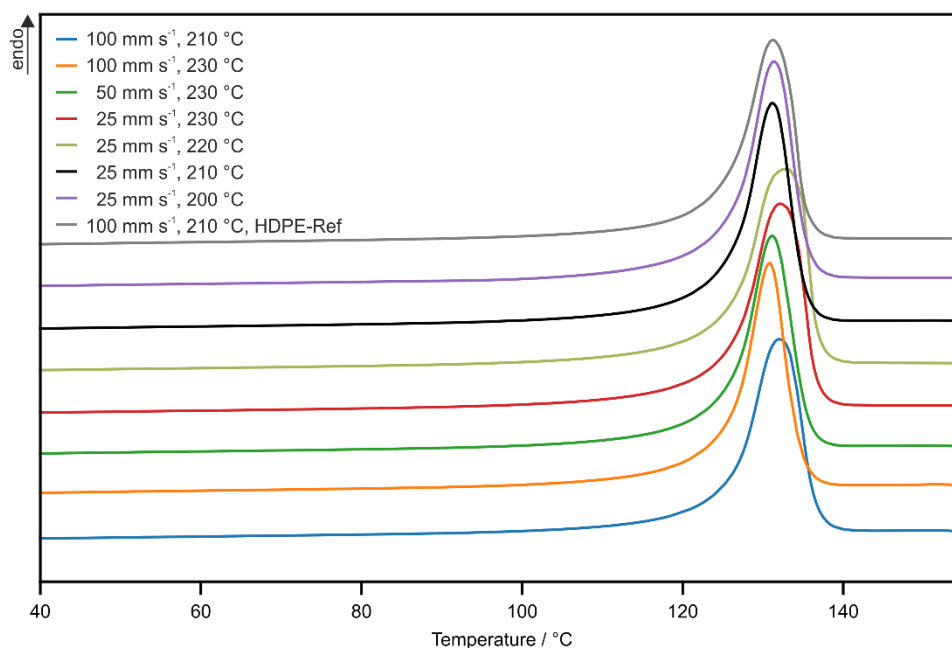
Figure S5: DSC traces of the first heat3D printed single-layered all-PE samples and benchmark HDPE reference.

No significant trend in heat flux can be observed for the variations in print temperature or print speed.

Crystallinity of the samples is determined by integration of the melt peak. Table S6 summarizes the results.

Table S6: Degree of crystallinity in HDPE and all-PE material processed by FFF with various print temperatures and print speeds obtained from DSC.

| Print Parameters	Melt temperature / °C	Crystallinity / %
HDPE 100 mm s^{-1} 210 °C	131.1	65
All-PE Material 100 mm s^{-1} 210 °C	131.8	63
All-PE Material 100mm s^{-1} 230 °C	130.9	66
All-PE Material 50mm s^{-1} 230 °C	131.1	66
All-PE Material 25 mm s^{-1} 230 °C	131.8	68
All-PE Material 25 mm s^{-1} 220 °C	132.4	68
All-PE Material 25 mm s^{-1} 210 °C	131.1	64
All-PE Material 25 mm s^{-1} 200 °C	131.4	67

Calculation of the thermal conductivity

For the simulation in *Comsol Multiphysics* the thermal conductivity of 3D printed all-PE material in print direction and perpendicular to the print direction is calculated according to Formula S8.

$$k = \alpha \, \varphi \, c_p$$

<div align="right">Formula S8</div>

The corresponding density φ of 0.913 ± 0.004 g cm^{-3} is measured with a helium pycnometer, the heat capacity c_p of 1.28 ± 0.03 J (g K)$^{-1}$ is determined by DSC and the thermal diffusivities α of 0.98 ± 0.05 mm^2 s^{-1} and 0.22 ± 0.01 mm^2 s^{-1} are known from lock-in thermography.
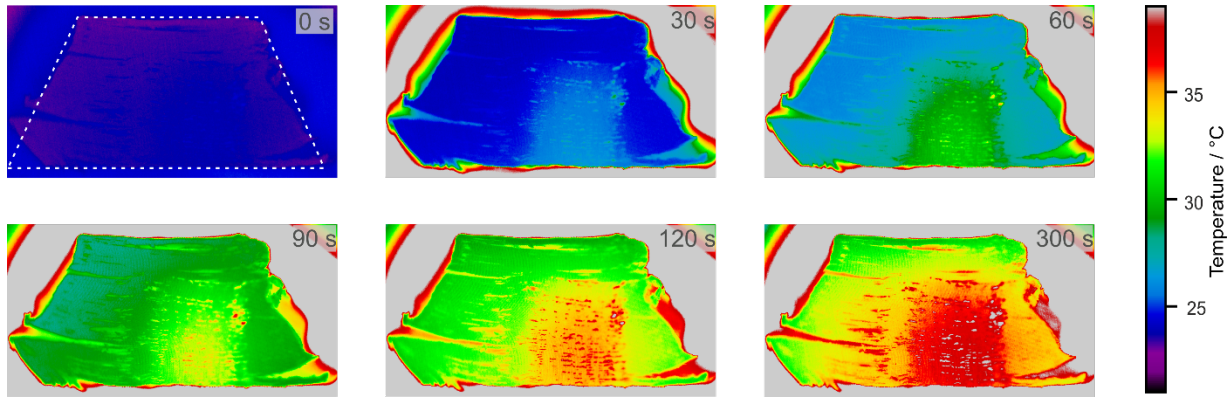
3D Printed All-PE Sample
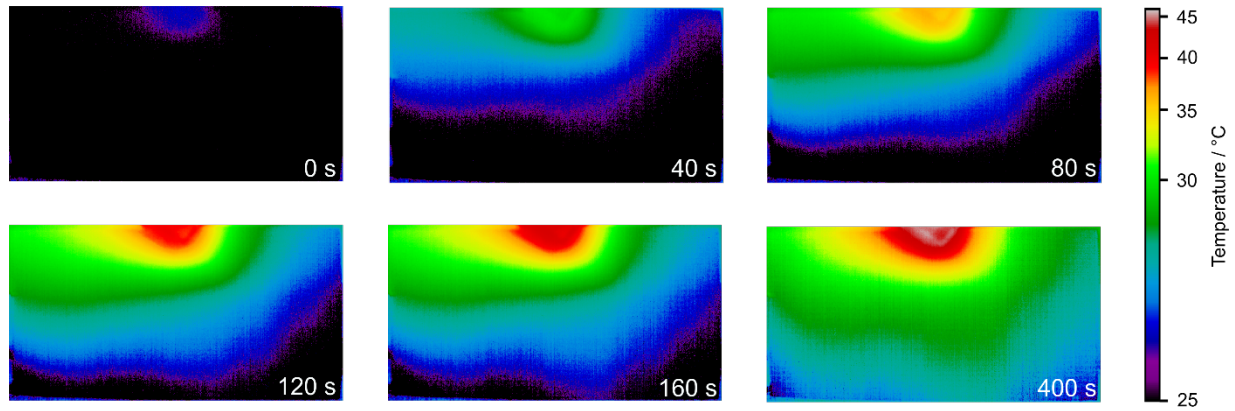
Figure S6: Evolution of the surface temperature of a single-layered sample, printed by FFF using two differing print directions and heated by a point-like heat source at 50 °C monitored *via* an IR camera.
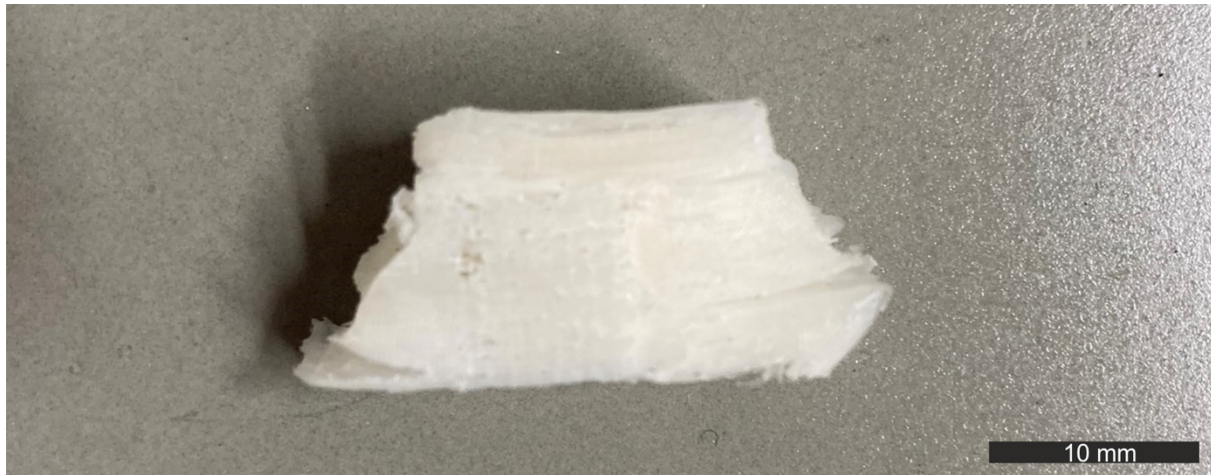
Figure S7: Image of the 3D printed all-PE sample used for demonstrating that defined temperature distributions are obtained by controlling the print direction.

Figure S8: Evolution of the surface temperature of a multi-layered sample, printed by FFF using two differing print directions and placed on a hot plate at 50 °C monitored *via* IR camera.

1. S. Krimm, C. Y. Liang and G. B. B. M. Sutherland, *The Journal of Chemical Physics*, 1956, **25**, 549-562.

2. S. Krimm, *Fortschritte der Hochpolymeren-Forschung*, 1960, **2**, 51-172.

3. A. R. Wedgewood and J. C. Seferis, *Pure Appl. Chem.*, 1983, **55**, 873-892.

4. S. Watanabe, J. Dybal, K. Tashiro and Y. Ozaki, *Polymer*, 2006, **47**, 2010-2017.

5. S. K. Markham, A. Mani, E. A. Korsakova, A. S. Korsakov, L. V. Zhukova, J. Bauer, C. Silien and S. A. M. Tofail, *J. Therm. Anal. Calorim.*, 2020, **142**, 1115-1122.

6. A. A. Alsaygh, J. Al-hamidi, F. D. Alsewailem, I. M. Al-Najjar and V. L. Kuznetsov, *Applied Petrochemical Research*, 2014, **4**, 79-84.

7. J. L. White, K. C. Dharod and E. S. Clark, *J. Appl. Polym. Sci.*, 1974, **18**, 2539-2568.

8. R. S. Stein, *Journal of Polymer Science*, 1958, **31**, 327-334.

9. C. G. Schirmeister, T. Hees, O. Dolynchuk, E. H. Licht, T. Thurn-Albrecht and R. Muelhaupt, *ACS Appl. Polym. Mater.*, 2021, **3**, 1675-1686.